Frenzel, M., et al., 2020, Halogens in hydrothermal sphalerite record origin of ore-forming fluids: Geology, v. 48, https://doi.org/10.1130/G47087.1

Appendix DR1

Accompanying the article: Halogens in hydrothermal sphalerite record origin of ore-forming fluids

By Max Frenzel*[1,2,3], Ashley Slattery[4], Ben Wade[4], Sarah Gilbert[4], Nigel J. Cook[3], Cristiana L. Ciobanu[3], Kathy Ehrig[5], Mathias Burisch[2], Max R. Verdugo-Ihl[3], Panagiotis Voudouris[6]

1 – Helmholtz-Zentrum Dresden Rossendorf, Institute Freiberg for Resource Technology, Chemnitzer Str. 40, 09599 Freiberg, Germany.

2 – Chair of Economic Geology and Petrology, Institute of Mineralogy, TU Bergakademie Freiberg, Brennhausgasse 14, 09599 Freiberg, Germany.

3 – School of Chemical Engineering and Advanced Materials, The University of Adelaide, SA 5005, Australia.

4 – Adelaide Microscopy, The University of Adelaide, SA 5005, Australia.

5 – BHP Olympic Dam, 10 Franklin St., Adelaide, 5000 SA, Australia.

6 – National and Kapodistrian Univ. of Athens, Dept. of Geology and Geoenvironment, University Campus-Zografou 15784 Athens, Greece.

*Corresponding author: m.frenzel@hzdr.de

33 # Contents

34

49

50

51

52

1. Materials and methods

1.1. Samples

Twelve samples from different hydrothermal ore deposits were selected to cover a wide range of formation conditions and check whether chlorine incorporation in sphalerite is a common phenomenon. A list of these samples is provided in Table DR1. Either polished thick sections (50 x 25 mm) or round mounts (25 mm) were prepared for further analyses.

Table DR1 – Sample overview

Sample ID	Deposit	Country	Deposit type[1]	Mineral association[2]	Texture	Reference(s)[3]
RX7319	Olympic Dam	Australia	IOCG	Sp-Bn-Qtz-Cc	Crystalline	Ehrig et al., 2012
BBH19†	Baita Bihor	Romania	Skarn	Sp-Bn-Gn	Crystalline	Cook et al., 2009
BS7b†	Baisoara	Romania	Skarn	Gn-Sp-Py-Cc	Crystalline	Cook et al., 2009
TM06_2†,[4]	Tres Marias	Mexico	MVT	Sp(-Py)	Crystalline	Saini-Eidukat et al., 2009
Toy-1†	Toyoha	Japan	Vein	Sp-Aspy-Qtz	Crystalline	Ohta, 1991
S4	Efemçukuru	Turkey	Vein	Qtz-Sp-Gn-Py-Cpy	Crystalline	Oyman et al., 2003
Zn99.2†	Zinkgruvan	Sweden	SHMS	Sp-Gn-Qtz	Crystalline	Jansson et al., 2017
TSU	Tsumeb	Namibia	MVT	Qtz-Cc-Sp-Gn-Cv-Bn	Crystalline	Lombaard et al., 1986
FG	Freiberg (kb)	Germany	Vein	Sp-Aspy-Qtz-Cc	Crystalline	Bauer et al., 2019
Li-HS-86[4]	Lisheen	Ireland	MVT	Py-Sp-Cc-Gn	Collof. / xtalline	Hitzman et al., 2002
65	Plaka	Greece	HTCR	Sp-Gn-Py-Qtz	Crystalline	Voudouris et al., 2008
MP	Mavres Petres	Greece	HTCR	Cc-Sp-Py-Aspy	Crystalline	Kalogeropoulos et al., 1989

[1]Deposit type abbreviations: IOCG – Iron-Oxide-Copper-Gold, MVT – Mississippi Valley-type, VHMS – Volcanic-hosted massive sulphide, HTCR – High-temperature carbonate replacement.

[2]Mineral abbreviations: Aspy – arsenopyrite, Bn – bornite, Cc – calcite, Cv – Covellite, Gn – galena, Py – pyrite, Qtz – quartz, Sp – sphalerite

[3]References are for deposit geology. Samples marked with † were also included in Cook et al. (2009).

[4]Samples contain several generations of sphalerite, which are denoted separately in the results section.

1.2. Electron-Probe Micro-Analysis (EPMA)

Prior to EPMA measurements, all samples were carbon-coated. Spot analyses and element X-ray maps were done according to the procedures described below.

Spot analyses

Quantitative compositions of sphalerite were determined using a Cameca SX-Five electron probe microanalyzer (EPMA), equipped with 5 tunable wavelength-dispersive spectrometers, located at Adelaide Microscopy (The University of Adelaide). The instrument is running PeakSite v6.2 software for microscope operation, and Probe for EPMA software (distributed by Probe Software Inc.) for all data acquisition and processing. Operating conditions utilized were 20 kV/40nA with a defocused beam size of 3µm. In order to attain better detection limits, the Cl Ka signal was measured on two separate spectrometers and aggregated utilizing the corresponding function in Probe for EPMA.

The full list of elements analysed along with primary and interference standards are presented in Tables DR2 to DR4. Matrix corrections of Armstrong-Love/Scott $\phi(\rho z)$ (Armstrong, 1988) and Henke MACs were used for data reduction. Due to the complexity of off-peak interferences in sulfide minerals, all elements were acquired using a multipoint background fit, excluding Cu, Ni and Cl which were acquired using a traditional 2-point linear fit.

84 **Table DR2** – EPMA setup for spot analyses of sphalerite

Element and Line	Diffracting Crystal (Sp#)	Background type/fit	kV/nA/spot size(µm)	Peak Count Time	Bkgd Count Times		# bkgd points acquired (Lo/Hi)	Standards*		Count Detection limit, 99% confidence (wt.%)
					Lo	Hi		Primary Standard	Interference Standards	
S Ka	LPET (1)	Multipoint	20/30/3	15	5	5	2/2	564	582	0.01
Cl Ka	LPET (1)	2-pt linear	20/30/3	60	60	60	1/1	545	566,562	0.003
Cd La	LPET (1)	Multipoint	20/30/3	15	5	5	0/4	561	566,560,568	0.03
Pb Ma	LPET (1)	Multipoint	20/30/3	15	5	5	4/3	566	556,562	0.03
Na Ka	TAP (2)	Multipoint	20/30/3	15	5	5	2/2	501	564	0.04
As La	TAP (2)	Multipoint	20/30/3	15	5	5	2/2	562	556	0.04
Se La	TAP (2)	Multipoint	20/30/3	15	5	5	2/3	568	562	0.03
Fe Ka	LLIF (3)	Multipoint	20/30/3	15	5	5	2/2	556	566	0.01
Cu Ka	LLIF (3)	2-pt linear	20/30/3	15	5	5	1/1	556		0.02
Mn Ka	LLIF (3)	Multipoint	20/30/3	15	5	5	2/2	557	562	0.01
Ga Ka	LLIF (3)	Multipoint	20/30/3	15	5	5	3/2	562	564	0.02
Ge Ka	LLIF (3)	Multipoint	20/30/3	15	5	5	2/2	592	564	0.04
Cl Ka	LPET (4)	2-pt linear	20/30/3	60	60	60	1/1	545	566,562	0.003
Ag La	LPET (4)	Multipoint	20/30/3	15	5	5	1/2	560	556,557	0.04
Sn La	LPET (4)	Multipoint	20/30/3	15	5	5	2/2	573	602,565	0.02
In La	LPET (4)	Multipoint	20/30/3	15	5	5	5/0	605	561,565	0.02
Zn Ka	LPET (5)	Multipoint	20/30/3	15	5	5	2/2	564		0.02
Hg La	LPET (5)	Multipoint	20/30/3	15	5	5	3/3	565	564	0.07
Ni Ka	LPET (5)	2-pt linear	20/30/3	15	5	5	1/1	536		0.01
Co Ka	LPET (5)	Multipoint	20/30/3	15	5	5	2/2	602		0.01

* Standard # refers to internal database. Full list of standards in Table DR4

85

86

87

88 **Table DR3** – Interference corrections for spot analyses of sphalerite

Element and Line	Overlapping element and order/interference correction standard					
	Interfering line	Int. std*	Interfering line	Int. std*	Interfering line	Int. std*
S Ka	Pb Ma (IV)	582				
Cl Ka	Pb Ma (IV)	566	As La (IV)	562		
Cd La	Pb Ma (IV)	566	Ag La (I)	560	Se La (IV)	568
Pb Ma	Fe Ka (III)	556	As La (V)	562		
Na Ka	Zn Ka (I)	564				
As La	Fe Ka (V)	556				
Se La	As La (I)	562				
Fe Ka	Pb Ma (II)	566				
Cu Ka						
Mn Ka	As La (II)	562				
Ga Ka	Zn Ka (I)	564				
Ge Ka	Zn Ka (I)	564				
Cl Ka	Pb Ma (IV)	566	As La (IV)	562		
Ag La	Cu Ka (III)	556	Mn Ka (II)	557		
Sn La	Co Ka (II)	602	Hg La (IV)	565		
In La	Cd La (I)	561	Hg La (III)	565		
Zn Ka						
Hg La	Zn Ka (I)	564				
Ni Ka						
Co Ka						

89 * Standard # refers to internal database. Full list of standards in Table DR4

Table DR4 – Standard information

Reference #	Mineral composition	Natural/Synthetic	Manufacturer
501	Albite	Natural	Astimex
545	Tugtupite	Natural	Astimex
556	Chalcopyrite	Natural	P&H and Associates
557	Rhodonite	Natural	P&H and Associates
560	Silver Telluride	Synthetic	P&H and Associates
561	Greenockite	Synthetic	P&H and Associates
562	Gallium Arsenide	Synthetic	P&H and Associates
564	Sphalerite	Natural	P&H and Associates
565	Cinnabar	Natural	P&H and Associates
566	Galena	Natural	P&H and Associates
568	Bismuth Selenide	Synthetic	P&H and Associates
573	Cassiterite	Natural	P&H and Associates
582	Lead	Synthetic	Astimex
592	Germanium	Synthetic	Astimex
602	Cobalt	Synthetic	Astimex
605	Indium	Synthetic	Astimex

Beam damage and element migration (e.g. S, Cl) was monitored by using the Time Dependent Intensity (TDI) correction feature of Probe for EPMA (e.g. Donovan and Rowe, 2005). The decay of x-ray counts over time is measured and modelled to return a t=0 intercept, and from this a concentration can be calculated. Upon visual inspection, the x-ray counts did not appear to decay over time and thus no correction was applied.

X-ray Maps

Sphalerite grains were x-ray mapped both qualitatively and quantitatively utilizing the same instrument at the University of Adelaide. Beam conditions were set at an accelerating voltage of 20kV and 90nA, utilizing a focused beam. Mapped area dimensions ranged from 20 - 5,000 µm in both x and y axes, at a pixel resolution of 1 – 10 µm. Pixel dwell time in all maps was set to 170ms. Maps ranged in acquisition time from ~2 – 12 h, depending on chosen pixel resolution and map size. Calibration and quantitative data reduction of maps was carried out in Probe for EPMA, distributed by Probe Software Inc. Color images of the maps were processed in Surfer 10® distributed by Golden Software. Calibration was performed on certified natural and synthetic standards from Astimex Ltd.

Sphalerite grains were quantitatively mapped for Cl, Zn, As, Pb, Cd, Fe, S, Cu, which required two passes. The first pass mapped for Cl Ka on multiple PET crystals (LPET1, PET2, LPET3), Zn Ka on LLIF3, and As Ka on LLIF5. The second pass mapped for Pb Ma (LPET1), Cd La (PET2), Fe Ka (LLIF3), S Ka (LPET4), and Cu Ka (LLIF5).

Map quantification was conducted in CalcImage, a module of Probe for EPMA. Background subtraction on the maps was performed via the Mean Atomic Number (MAN) background correction (Donovan and Tingle, 1996; Donovan et al., 2016), omitting the need for a second pass "off-peak" map acquisition. Following this, each pixel goes through full $\phi(\rho z)$ corrected quantification identical to traditional spot analysis.

1.3. Laser ablation-inductively coupled plasma-mass spectrometry (LA-ICP-MS)

Sphalerite was analyzed in all samples using an ESI NWR213 solid state laser coupled to an Agilent 7900 ICP-MS at the University of Adelaide. The system uses He as the carrier gas in the sample chamber, which is mixed with Ar for transport to the ICP-MS. A minimum of 5 spot analyses were performed on each mineral generation in each sample. The following isotopes were monitored during each measurement (30s background, 50s ablation): ^{23}Na, ^{35}Cl, ^{55}Mn, ^{57}Fe, ^{59}Co, ^{60}Ni, ^{63}Cu, ^{66}Zn, ^{69}Ga, ^{72}Ge, ^{73}Ge, ^{75}As, ^{77}Se, ^{79}Br, ^{81}Br, ^{107}Ag, ^{111}Cd, ^{113}In, ^{115}In, ^{118}Sn, ^{121}Sb, ^{125}Te, ^{202}Hg, ^{205}Tl, ^{208}Pb and ^{209}Bi. Ablation spot size was generally 50 µm. For sample S4, a smaller spot size (25 µm) had to be used to avoid abundant inclusions of galena, while in TM06.2 analyses were conducted with a larger spot size (110 µm) to enhance count rates for the Cl and Br isotopes. Some larger spots (110 µm) were also measured on BS7b and Li-HS-86, as detailed in Appendix C. In general, an ablation pulse frequency of 10 Hz, and fluence of 3.5 J/cm^2 were used.

Data reduction was done using the Iolite software package (Paton et al., 2011). To convert the measured signals to concentrations, ^{66}Zn was used as the internal standard element. MASS-1 (Wilson et al., 2002) was used as the external standard for Na, Mn, Fe, Co, Ni, Cu, Ga, Ge, As, Se, Ag, Cd, In, Sn, Sb, Te, Hg, Tl, Pb and Bi, and NIST SRM 610 (NIST, 2012) as the external standard for Cl and Br. Average Zn concentrations for each sphalerite generation in each sample were taken from EPMA measurements. A block of two to three standard measurements was inserted before and after every 20 to 30 sample measurements. Off-line corrections were made for the isobaric interferences of ^{113}Cd on ^{113}In, and ^{115}Sn on ^{115}In in both the samples and the standard, using raw count rates and the natural abundance ratios of the relevant isotopes. Interferences of ^{56}Fe^{16}O and ^{57}Fe^{16}O (cf. Belissont et al., 2014) on ^{72}Ge and ^{73}Ge, respectively, were monitored by comparing the measured abundance ratio of ^{72}Ge to ^{73}Ge in the sample to the natural ratio expected for the two isotopes. If significant deviations (more than 50 rel.%) of ^{72}Ge/^{73}Ge from the natural value of 3.5 occurred, the measurement was designated as below detection limit, with the higher of the two reported concentration values as the detection limit. In general, interferences did not appear to be a problem, as also noted by Belissont et al. (2014). Even in Fe-rich, Ge-poor sphalerites, spurious concentrations produced by the interference of Fe-O species on Ge never exceeded 0.5 µg/g. The official reference value of 58 ppm Ge was used for the MASS-1 standard (cf. Belissont et al., 2014), and count rates on MASS-1 always showed the correct ^{72}Ge/^{73}Ge ratio (to within 10 rel.% of the expected natural value).

A particular challenge for the LA-ICP-MS measurement of Cl in a sphalerite matrix is the interference of ^{70}Zn^{2+} on ^{35}Cl^{+} (Fig. DR1a). Other matrix-related interferences may also be present (for Na, Cl, Br; e.g. Hammerli et al. 2013). To determine the magnitude of these interferences, two to three blank measurements of a pure synthetic sphalerite (> 99.995% ZnS, Alfa Aesar; no measurable Cl or Br content) were added to each standard block. These showed that appreciable spurious blank signals are only present for Cl, but not Na and Br (Fig. DR1a). Therefore, sample measurements of Cl were subsequently corrected offline for the spurious concentrations determined in the blank, but not Na and Br. Correction was done by subtracting the Cl concentration measured in the blank from the measured concentrations of Cl in the samples.

Hammerli et al. (2013) further reported the occurrence of appreciable unexplained spurious Br concentrations on ablation of a blank (quartz in their case) when measuring the ^{79}Br isotope, as compared to ^{81}Br. Such spurious signals did not occur in the measurements conducted for the present study, and we therefore suggest that the observations of Hammerli et al. (2013) may have been related to the specific equipment they used. Reported Br concentrations are therefore equal to the mean of the measurements for the two isotopes. We also did not observe spurious signals due to re-worked halogens from the ablation cell, as described in Seo et al. (2011).

Some further difficulty in the measurement of Cl and Br by LA-ICP-MS arises from uncertainties regarding the absolute concentrations of Cl and Br in NIST SRM 610 (NIST, 2012). In the present study we used the value of 820 ppm for Cl reported by Marks et al. (2016) based on their EPMA and TXRF

analyses. This gives excellent agreement between our EPMA and LA-ICP-MS results (Fig. DR2a below). For Br we used the value of 33 ppm reported by Seo et al. (2011), since this is the only available value determined by LA-ICP-MS. In our opinion, the large inconsistencies in Br values determined on NIST SRM 610 and 612 by different bulk analytical techniques as cited in Marks et al. (2016) are an indicator for unreliable results. Furthermore, we do not expect the value reported by Seo et al. (2011) to be affected by the ArK interferences described by Hammerli et al. (2013), as suggested by Marks et al. (2016), since NIST SRM 610 does not contain significant K (< 0.05 wt.%; Marks et al., 2016). The absence of ArK interferences has also been demonstrated by Seo and Zajacz (2016).

Measurement results, including standard measurements, uncertainties and detection limits for all elements are reported in Appendix DR3. Since the Iolite software produces unrealistically low detection limits in cases where background counts are below the minimum count rate (50 cps in our case), detection limits for the affected elements were estimated assuming a count detection limit of two times the minimum count rate, i.e. 100 cps. This procedure was applied to the following elements: Co, Ni, Cu, Ga, Ge, Se, Ag, Cd, In, Sn, Sb, Tl and Pb. For Na, Cl and Br, background counts were generally high, and the detection limits given by Iolite were therefore considered reliable.

1.4. Scanning transmission electron microscopy (STEM)

To examine the nanostructure of Cl-rich sphalerite, two TEM foils each were cut from Cl-rich areas on the polished sections of samples BS7b and Li-HS-86, and attached to standard copper TEM grids, using a FEI-Helios nanoLab dual focused ion beam and scanning electron microscope (FIB-SEM). The procedures outlined in Ciobanu et al. (2011) were followed in the extraction and thinning (to <100 nm) of TEM foils by ion beam milling using Ga ions.

Foils were first examined using a Philips CM200 transmission electron microscope (TEM) equipped with a LaB_6 source, double-tilt holder and Gatan digital camera, operated at 200 kV, to obtain selected area electron diffraction (SAED) patterns on different areas of the sample foils. Image analysis was performed using DigitalMicrograph^{TM} 3.11.1. SAED patterns were indexed manually. All areas were confirmed to be sphalerite.

The foils were subsequently examined in high-angle annular darkfield (HAADF) scanning mode with a FEI Titan Themis 80-200 ultra-high-resolution TEM. An operation voltage of 200 kV was used. The instrument features an X-FEG Schottky source and super-X EDX geometry, providing symmetric EDX detection with an effective solid angle of 0.8 Sr. Probe correction delivered a spatial resolution of ~ 1 nm for imaging and EDX mapping. An inner collection angle greater than 50mrad was used for HAADF imaging with a Fischione detector. Imaging, EDX-spot analyses and EDX-mappings (Zn, S, Fe, Pb, Cu, Cl) were conducted. All instruments are housed at the University of Adelaide.

2. Detailed results

2.1. EPMA spot analyses

Detailed results for each measurement point on each sample, including uncertainties (1 standard error) and count detection limits (99% confidence) are provided in Appendix B. Data summaries are provided in Tables DR5 to DR6 below, using median values and 80% probability ranges.

It is apparent from this summary, that sphalerite compositions span the entire relevant range in possible Fe, Mn and Cd concentrations for hydrothermal sphalerite (cf. Cook et al., 2009; Frenzel et al., 2016). For other common trace elements (Ge, In, Co, Ag etc.), detection limits were too low for reliable measurement in most samples. We note, however, that the highest values recorded for these

elements in some samples are not atypical. Importantly, Cl concentrations were consistently measurable in 3 out of the 12 samples (BS7b, TM06.2, Li-HS-86; Table DR5), reaching values up to 100s or 1,000s of µg/g. In addition, one sample showed a small number of analyses above 100 µg/g (Toy-1), and a further two samples (RX7319, BBH19) showed some values just above the detection limit.

From the EPMA data alone, it does not appear that high Cl concentrations in a sample systematically occur together with high concentrations of any of the other measured elements. However, Mn concentrations appear to be consistently low in Cl-rich samples.

2.2. LA-ICP-MS spot analyses

Data on each individual measurement point are provided in Appendix C, including analytical uncertainties (2 standard errors) and count detection limits (99 % confidence; µg/g). Data summaries are provided in Tables DR7 and DR8.

In addition to Cl, Na and Br were consistently present in all Cl-rich samples (Fig. DR1, Table DR7), and absent in those without measurable Cl (Table DR7). Ablation traces of all three elements were generally smooth, but inclusions are also present in some cases (e.g. Fig. DR1d). While detection limits for Cl were not as good as for EPMA measurements, there is excellent agreement between the mean Cl concentrations determined in different samples by the two methods (Fig. DR2a). For individual spot analyses, there is some scatter, however. This is probably due to differences in the analysed volumes for the two techniques (3 µm spots for EPMA, ≥20 µm for LA-ICP-MS) in combination with strong oscillatory zonation of the sample (Fig. DR2b).

The concentrations of the other trace elements (Co, Ga, Ge etc.) are in the general range expected for natural sphalerite (cf. Cook et al., 2009; Frenzel et al., 2016). Some relationships with Cl are already suggested by the table, e.g. Tl only shows high (measurable) values in the Cl-rich samples. Similarly, Ge is high in all Cl-rich samples, but generally low in those without measurable Cl. Correlations of Cl with other elements at different hierarchical levels are examined more closely in the next section.

2.3. Correlation of Cl and Br with other trace elements

The relationships of Cl (and Br) with other trace elements in the investigated samples were studied at two hierarchical levels: first, across different sphalerite types, and second, within types.

For the investigation of cross-type trends, a simple student's t-test was conducted to test for statistically significant differences in trace element concentrations between the Cl-rich and Cl-poor sphalerite types. This showed that significant differences exist for Na, Tl, Ge and Mn, as well as inferred formation temperature (from the GGIMFis thermometer; cf. Frenzel et al., 2016). For Cd, Fe, Co, Ga etc., no significant differences are apparent. These trends are illustrated in Fig. DR3, which shows plots of mean trace element concentrations within the sphalerite types against mean Cl concentrations determined by EPMA (geometric means). While Na, Tl and Ge tend to be higher, on average, in the Cl-rich sphalerites, Mn and inferred formation temperature tend to be lower. Thus, high Cl concentrations primarily appear to be a feature of many, but not all, low-temperature sphalerites. Since Br concentrations closely mirror Cl, the same is true for this element. Interestingly, the two halogens generally appear to be accompanied by Na as another non-standard trace element, albeit not in stoichiometric proportions (cf. Table DR7).

For the investigation of within-type trends, the correlation coefficients of Cl with the other trace elements in the Cl-rich sphalerites were compiled (Table DR9). From this compilation, it is clear that

behavior varies between types. However, we note that the correlation coefficients of Cl with the monovalent cations, particularly Na and Tl, tend to be positive. There is also a strong correlation between Cl and Br in the two sphalerites with the highest Cl concentrations, BS7b and Li-HS-86 (II). Relationships with other trace elements are more ambiguous, and to uncover any general trends will

likely require the analysis of a larger number of samples in future studies. Fig. DR4 shows a selection of 6 scatter plots corresponding to the correlations illustrated in Table DR9.

Finally, Fig. DR5 shows Cl+Br concentrations as a function of the approximate net negative lattice charge caused by the cationic elements in the sphalerite (cf. Belissont et al. 2014). From this figure it is clear that approximate charge balance is only maintained in sample BS7b, where Cl substitution appears to roughly offset the net negative charge introduced into the sphalerite lattice by substitution of Cu, Ag, Tl and Na for Zn. In sample Li-HS-86 (sphalerite II), on the other hand, excess Cl appears to be present. The same is true for sample TM06.2 (sphalerite I). Also note that the charge balance calculation for Li-HS-86 was done without Cu, since this was assumed to be hosted in Cu-Pb-Cl inclusions instead (cf. section A2.6. below).

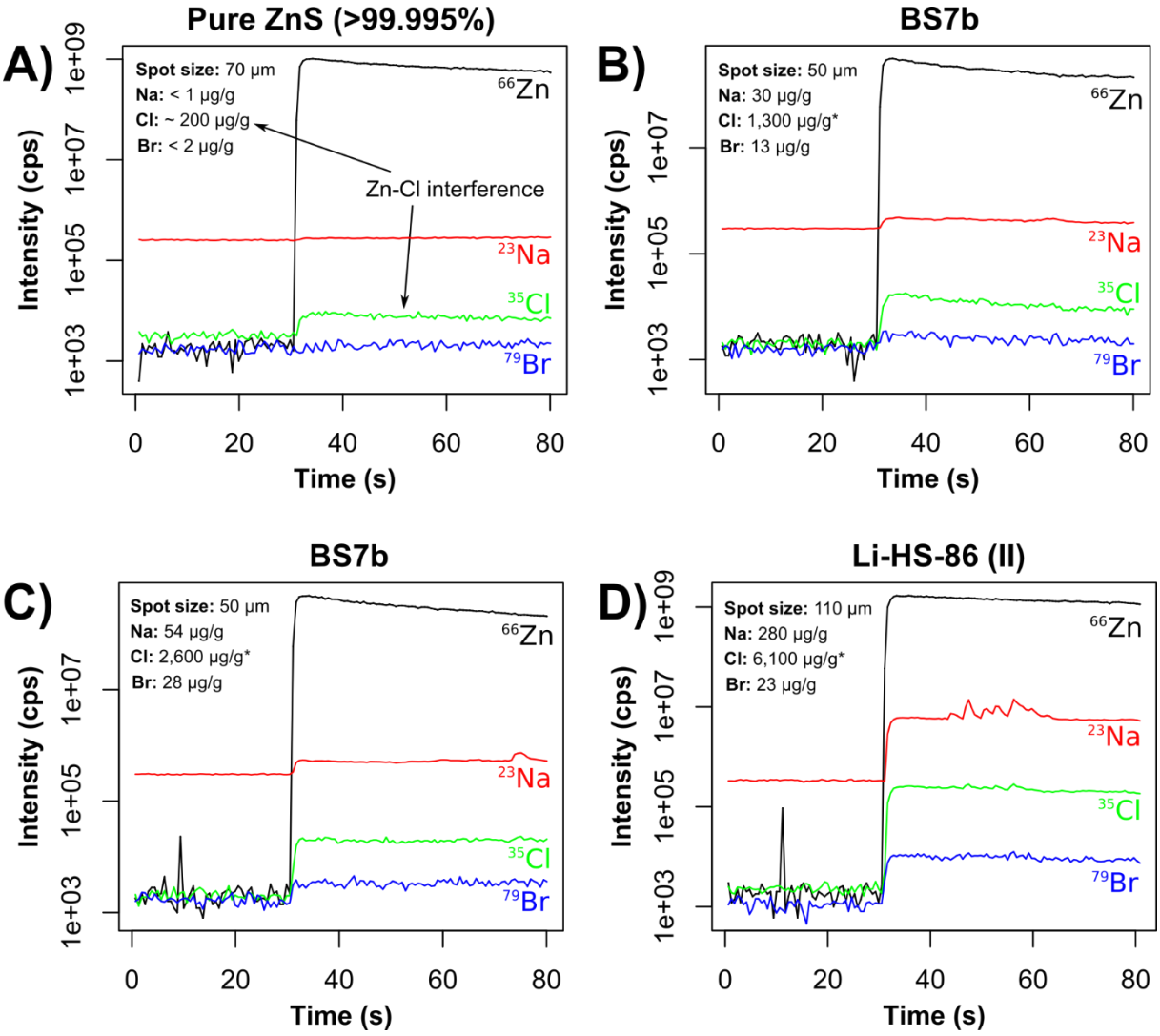

Fig. DR1. Ablation traces of ^{66}Zn, ^{23}Na, ^{35}Cl and ^{79}Br for different samples, clearly showing the presence of Na and Br in addition to Cl in Cl-rich samples. A) Pure synthetic ZnS, with clearly visible spurious ^{35}Cl signal from doubly charged ^{70}Zn, B) and C) analysis spots on BS7b with different Cl concentrations; D) extremely Cl-rich analysis spot on sample Li-HS-86, sphalerite II (colloform). Calculated Cl concentrations in panels B) to D) are corrected for the interference from ^{70}Zn.

Table DR5 – Summary statistics for EPMA spot analyses (median values)

Sample ID	n	S (wt.%)	Pb (wt.%)	Fe (wt.%)	Cu (wt.%)	Mn (wt.%)	Ag (wt.%)	Zn (wt.%)	Cd (wt.%)	In (wt.%)	Co (wt.%)	Cl (µg/g)	Ge (wt.%)	Sum (wt.%)*
Li-HS-86 (II)	31	32.6	0.55	0.57	0.12	<0.01	<0.04	65.1	0.10	<0.02	<0.02	4,900	<0.04	99.5
BS7b	8	31.7	0.35	0.09	0.36	<0.01	<0.04	63.8	2.1	<0.02	<0.01	1,200	<0.04	99.0
TM06.2 (I)	16	33.3	0.20	9.4	0.03	<0.01	<0.04	56.1	0.32	<0.02	0.01	230	0.07	99.8
Li-HS-86 (I)	20	32.8	0.17	0.62	0.07	<0.01	<0.04	66.4	0.07	<0.02	<0.02	180	<0.04	100.3
TM06.2 (II)	5	33.0	0.09	1.6	0.02	<0.01	<0.04	64.5	0.23	<0.02	0.01	46	<0.04	99.8
Toy-1	9	33.0	0.08	4.4	0.30	0.02	0.10	58.2	0.56	0.18	<0.01	<30	<0.04	100.0
RX7319	23	32.9	0.08	0.09	0.10	<0.01	<0.04	66.9	0.14	<0.02	<0.01	<30	<0.04	100.3
BBH19	11	32.8	0.10	0.08	0.16	0.11	<0.04	66.3	0.46	0.12	0.13	<30	<0.04	100.2
S4	10	32.7	0.08	4.3	0.85	1.4	<0.04	60.5	0.12	<0.02	<0.01	<30	<0.04	99.5
Zn99.2	31	33.9	0.09	3.5	<0.02	0.06	<0.04	63.1	0.28	<0.02	0.02	<30	<0.04	100.9
TSU	20	32.8	0.08	<0.01	0.12	0.18	<0.04	66.1	1.0	<0.02	<0.01	<30	<0.04	100.4
FG	22	33.0	0.05	9.8	0.05	0.46	<0.04	55.8	0.41	0.03	0.02	<30	<0.04	99.8
65	15	33.0	0.07	12.0	0.04	0.45	<0.04	53.3	0.19	<0.02	0.02	<30	<0.04	99.1
MP	26	33.2	0.06	10.6	<0.02	0.65	<0.04	54.8	0.31	<0.02	<0.01	<30	<0.04	99.6

*Median of sum totals for individual measurements; not equal to sum of median values for individual elements

Table DR6 – Summary statistics for EPMA spot analyses (ranges: 10th and 90th percentiles for n ≥ 10, otherwise overall ranges)

Sample ID	N	S (wt.%)	Pb (wt.%)	Fe (wt.%)	Cu (wt.%)	Mn (wt.%)	Ag (wt.%)	Zn (wt.%)	Cd (wt.%)	In (wt.%)	Co (wt.%)	Cl (µg/g)	Ge (wt.%)
Li-HS-86 (II)	31	32.0 – 33.0	0.17 – 0.88	0.36 – 0.70	0.07 – 0.57	<0.01 – 0.05	<0.04 – 0.05	64.0 – 65.7	0.06 – 0.13	<0.02 – 0.03	≤0.01	1,400 – 7,900	<0.04
BS7b	8	31.4 – 32.2	0.12 – 0.49	0.06 – 1.1	<0.02 – 0.96	<0.01	<0.04	62.6 – 65.9	<0.03 – 3.6	<0.02 – 0.05	<0.01 – 0.02	1,000 – 3,800	<0.04
TM06.2 (I)	16	33.1 – 33.6	0.14 – 0.31	6.5 – 12.0	<0.02 – 0.05	<0.01	<0.04	53.4 – 59.7	0.24 – 0.46	≤0.02	<0.01 – 0.03	110 – 390	0.04 – 0.11
Li-HS-86 (I)	20	32.6 – 33.0	0.07 – 0.46	0.28 – 1.28	<0.02 – 0.60	≤0.01	<0.04	64.7 – 67.0	0.04 – 0.11	<0.02 – 0.03	<0.01 – 0.02	<30 – 1,600	<0.04
TM06.2 (II)	5	32.7 – 33.2	0.07 – 0.10	0.86 – 5.6	<0.02 – 0.04	<0.01	<0.04	60.5 – 66.0	0.13 – 0.47	<0.02 – 0.03	<0.01 - 0.02	<30 - 170	<0.04 – 0.10
Toy-1	9	32.7 – 33.1	0.05 – 0.13	3.2 – 7.1	0.19 – 2.3	<0.01 – 0.03	<0.04 – 0.27	53.2 – 62.6	0.07 – 1.2	<0.02 – 4.3	<0.01 – 0.02	<30 – 300	<0.04
RX7319	23	32.7 – 33.0	0.05 – 0.12	0.04 – 0.28	0.05 – 0.57	<0.01	<0.04	66.5 – 67.1	0.10 – 0.17	<0.02 – 0.03	0.01 – 0.03	<30 – 46	<0.04
BBH19	11	32.6 – 32.9	0.04 – 0.12	0.06 – 0.13	0.08 – 0.29	0.07 – 0.14	<0.04	66.1 – 66.4	0.44 – 0.51	0.09 – 0.14	0.09 – 0.17	<30 – 52	<0.04
S4	10	32.0 – 33.0	0.05 – 0.20	2.3 – 5.4	0.13 – 2.1	0.38 – 1.7	<0.04 – 0.80	57.8 – 61.6	0.07 – 0.18	<0.02 – 0.03	<0.01 – 0.02	<30	<0.04
Zn99.2	31	33.7 – 34.0	0.05 – 0.13	3.4 – 3.5	<0.02 – 0.03	0.05 – 0.07	<0.04	62.8 – 63.3	0.24 – 0.33	<0.02 – 0.03	0.02 – 0.03	<30	<0.04
TSU	20	32.7 – 32.9	0.07 – 0.12	<0.01 – 0.06	0.04 – 0.30	0.16 – 0.18	<0.04	65.8 – 66.4	0.99 – 1.1	<0.02	<0.01	<30	<0.04
FG	22	32.9 – 33.2	<0.03 – 0.08	9.6 – 9.9	0.03 – 0.07	0.44 – 0.48	<0.04	55.7 – 56.1	0.37 – 0.44	<0.02 – 0.07	<0.01 – 0.03	≤30	<0.04
65	15	32.9 – 33.0	0.04 – 0.10	11.7 – 12.7	<0.02 – 0.20	0.37 – 0.58	<0.04	52.5 – 53.6	0.15 – 0.24	<0.02 – 0.03	<0.01 – 0.03	<30	<0.04
MP	26	33.1 – 33.4	0.04 – 0.09	5.7 – 11.3	<0.02 – 0.03	0.22 – 1.12	<0.04	54.1 – 59.5	0.26 – 0.36	<0.02 – 0.04	<0.01 – 0.03	<30	<0.04

Table DR7 – Summary statistics for LA-ICP-MS data (median values)

Sample ID	n	Na (µg/g)	Cl (µg/g)	Br (µg/g)	Mn (µg/g)	Fe (µg/g)	Co (µg/g)	Cu (µg/g)	Ga (µg/g)	Ge (µg/g)	Ag (µg/g)	Cd (µg/g)	In (µg/g)	Tl (µg/g)	PC1*	T (°C)*
Li-HS-86 (II)	16	310#	5,800#	23#	18#	5,300	0.23#	2,800#	0.02	190	140#	960	<0.02	780#	0.55#	178
BS7b	25	64#	2,300	21	2.9#	290#	0.91#	6,900#	12#	5.6#	190#	29,900#	42#	21#	1.50#	127#
TM06.2 (I)	15	17#	210	3.1	44	85,200	0.33	10#	0.95	860	1.5	4,800	0.09	120	0.14	200
Li-HS-86 (I)	24	<5	<400	<10	3.7#	5,000#	1.3#	290#	<0.4	34#	13#	800	<0.1	0.8#	0.93	158
TM06.2 (II)	6	--#	70	2.5	9.2	28,500	0.23	--#	19	190	0.67	3,400	0.004	27	1.45	129
Toy-1**	18	n.d.	n.d.	n.d.	78	48,000	0.89	30,900	190	0.95	3,600	8,900	17,000	0.14	-1.38	283
RX7319	26	<8	<140	n.d.	1.0#	400#	130	570#	<0.06	<0.7	0.52#	700	0.18	<0.02	0.63#	174
BBH19	11	<1	<80	<3	1,100	920#	1,100	1,300#	0.39	<0.7	3.6#	2,800	630	<0.02	-1.53#	291
S4	17	<7	<400	<20	13,500	43,700	0.44	15,600#	2.1	<3	93#	770	6.0	<0.2	-2.16	325
Zn99.2	41	<3	<90	n.d.	480	31,900	120	2.8	1.1	<0.7	4.1	1,100	0.20	<0.02	-1.54	292
TSU	22	<3	<100	n.d.	1,500	66#	1.2#	820#	150	43#	1.9#	4,600	0.82	0.13#	2.04#	97
FG	20	<5	<100	n.d.	3,600	81,000	14	130#	<0.06	<0.7	1.9#	1,800	150	<0.02	-3.67	408
65	20	<1	<60	<2	3,800	100,000	4.3#	160#	1.5	<0.7	4.9#	1,400	1.1#	<0.02	-2.50#	344
MP	31	<1#	<60#	<4#	5,800	95,600#	<0.06	120#	19#	<0.7	1.6#	2,200	96	<0.02#	-2.42#	340

Note: n gives number of total measurements. Means do not include measurements with inclusions of the respective element, so no. of reliable measurements for individual elements in a sample can be smaller than n. This also applies to PC1 values. Such values are marked with #. Where all measurements were affected by inclusions, this is marked with "--"; n.d. – not determined.

For Li-HS-86 (II), reported values correspond to measurements with larger spot sizes (50 and 110 µm) only.

* – Calculated according to Frenzel et al. (2016); ** – Data from Cook et al. (2009).

Table DR8 – Summary statistics for LA-ICP-MS data (ranges: 10th and 90th percentiles for n ≥ 10, otherwise overall range) cont. on next page for In, Tl, PC1 and T

Sample ID	n	Na (µg/g)	Cl (µg/g)	Br (µg/g)	Mn (µg/g)	Fe (µg/g)	Co (µg/g)	Cu (µg/g)	Ga (µg/g)	Ge (µg/g)	Ag (µg/g)	Cd (µg/g)
Li-HS-86 (II)	16	8.7 – 680#	1,100 – 7,900#	6.2 – 29#	3.1 – 250#	3,500 – 6,800	0.12 – 1.3#	620 – 7,000#	<0.06 – 0.17	120 – 300	100 – 380#	870 – 1,100
BS7b	25	50 – 130#	1,100 – 4,500	8.2 – 37	1.6 – 39#	240 – 5,200#	0.89 – 57#	300 – 8,000#	6.8 – 67#	1.6 – 12#	9.2 – 270#	1,300 – 47,000#
TM06.2 (I)	15	16 – 26#	110 – 280	2.9 – 3.7	38 – 47	76,200 – 103,000	0.31 – 0.35	1.1 – 80.9#	0.14 – 3.4	790 – 940	0.60 – 3.5	3,500 – 5,800
Li-HS-86 (I)	24	<5 – 26	<400 – 1,400	<10	0.82 – 94#	2,700 – 6,700#	0.52 – 2.6#	53 – 1,400#	<0.4 – 4.6	10 – 190#	1.6 – 160#	570 – 1,100
TM06.2 (II)	6	--#	9 – 100	2.3 – 3.2	5.6 – 15	16,700 – 36,500	0.09 – 0.27	--#	8.1 – 41	130 – 220	0.51 – 1.0	2,800 – 5,100
Toy-1**	18	n.d.	n.d.	n.d.	64 – 210	34,600 – 67,200	0.01 – 44	2,300 – 40,200	83 – 510	0.8 – 3.7	730 – 23,700	6,500 – 12,700
RX7319	26	<8	<70	n.d.	0.6 – 4.6#	280 – 490#	120 – 140	210 – 1,600#	<0.06	<0.7	0.4 – 1.2#	660 – 730
BBH19	11	<1	<80	<3	660 – 1,200	510 – 1,300#	700 – 1,300	620 – 2,900#	<0.06 – 0.70	<0.7	1.7 – 20#	2,700 – 3,000
S4	17	<7	<400	<20	8,000 – 15,500	31,300 – 50,500	<0.3 – 0.77	1,200 – 27,400#	1.3 – 4.1	<3	13 – 170#	650 – 1,000
Zn99.2	41	<3 – 4.8	<90	n.d.	480 – 490	31,500 – 32,200	120 – 130	1.8 – 5.4	1.0 – 1.2	<0.7	2.8 – 6.4	1,100 – 1,200
TSU	22	<3 – 10	<100	n.d.	1,500 – 1,600	34 – 170#	0.25 – 2.0#	210 – 1,400#	140 – 160	<0.7 – 220#	0.81 – 4.3#	3,900 – 6,000
FG	20	<5	<100	n.d.	3,400 – 3,700	79,100 – 84,500	13 – 15	110 – 2,600#	<0.06	<0.7	1.6 – 5.4#	1,600 – 1,900
65	20	<1 - 10	<60	<2	3,000 – 4,500	96,700 – 104,000	2.2 – 5.9#	45 – 1,000#	0.90 – 2.5	<0.7	2.2 – 17#	1,300 – 1,600
MP	31	<1 – 2.8#	<60#	<4#	1,800 – 10,000	52,700 – 105,000#	<0.06	42 – 220#	9.4 – 56#	<0.7	0.97 – 4.5#	2,000 – 2,400

Note: same symbols and footnotes apply as for Table DR7 above.

Table DR8 (cont'd)

Sample ID	n	In (µg/g)	Tl (µg/g)	PC1*	T (°C)*
Li-HS-86 (II)	16	<0.02	12 – 1,400[#]	0.16 – 1.00[#]	153 – 199
BS7b	25	0.17 – 390[#]	10 – 34[#]	1.04 – 1.66[#]	118 – 151
TM06.2 (II)	15	0.01 – 0.51	98 – 150	-0.01 – 0.31	191 – 208
Li-HS-86 (I)	24	<0.1	<0.2 – 23[#]	0.24 – 1.72	115 – 195
TM06.2 (I)	6	<0.002 – 0.08	22 – 43	1.30 – 1.82	109 – 137
Toy-1	18	370 – 65,100	0.03 – 0.54	(-1.73) – (-0.75)	249 – 302
RX7319	26	0.1 – 0.3	<0.02	0.46 – 0.89[#]	160 – 183
BBH19	11	540 – 730	<0.02	(-1.94) – (-1.34)[#]	281 – 314
S4	17	<1 – 10	<0.2	(-2.40) – (-1.79)	305 – 338
Zn99.2	41	0.19 – 0.21	<0.02	(-1.57) – (-1.52)	291 – 293
TSU	22	0.76 – 0.91	0.04 – 0.39[#]	1.43 – 2.27[#]	84 – 130
FG	20	130 – 340	<0.02	(-3.75) – (-3.63)	406 – 412
65	20	<0.02 – 2.4[#]	<0.02	(-2.63) – (-2.08)[#]	320 – 350
MP	31	14 – 220	<0.02 – 0.04[#]	(-2.60) – (-2.05)[#]	320 – 349

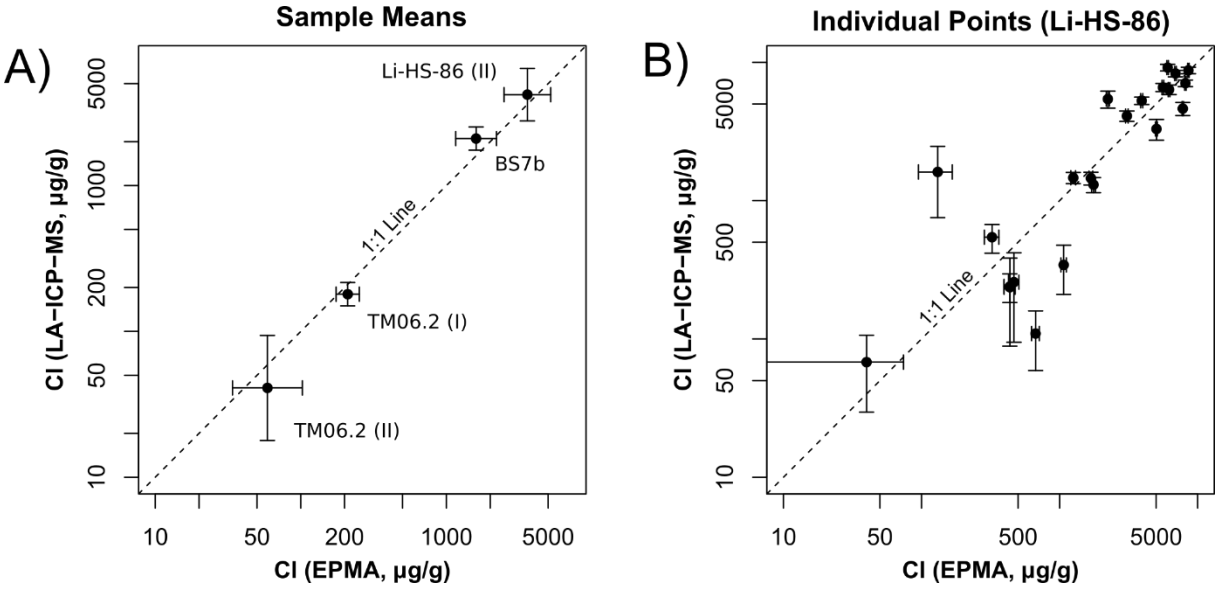

Fig. DR2: Comparison between Cl concentrations determined by LA-ICP-MS and EPMA: A) geometric means (including 95% confidence intervals) for individual sphalerite types, B) individual measurement points (also with 95 % confidence intervals) on sample Li-HS-86. Note excellent correspondence of determined values in panel A). Scatter in panel B) is likely a function of different analysis volumes for the two methods paired with relatively strong zonation of the sample (cf. Fig. DR6).

Table DR9 – Correlation coefficients (R) for Cl with other trace elements within samples

	BS7b	Li-HS-86 (II)	TM06_2 (I)	TM06_2 (II)
Monovalent cations				
Na	0.65	**0.91**	**0.89**	--
Tl	0.25	**0.91**	**0.88**	0.63
Cu	**0.90**	0.73	-0.55	--
Ag	**0.89**	0.09	-0.66	-0.50
Divalent cations				
Mn	**-0.86**	0.48	-0.26	0.57
Fe	**-0.89**	0.59	0.28	0.67
Co	**-0.88**	-0.74	0.37	0.24
Cd	**0.85**	-0.28	-0.47	-0.43
Tri- / Tetravalent cations				
Ga	**-0.86**	-0.26	-0.59	-0.07
Ge	-0.49	0.52	-0.40	0.63
In	0.79	--	-0.56	--
Monovalent anions				
Br	**0.98**	**0.99**	0.29	0.64

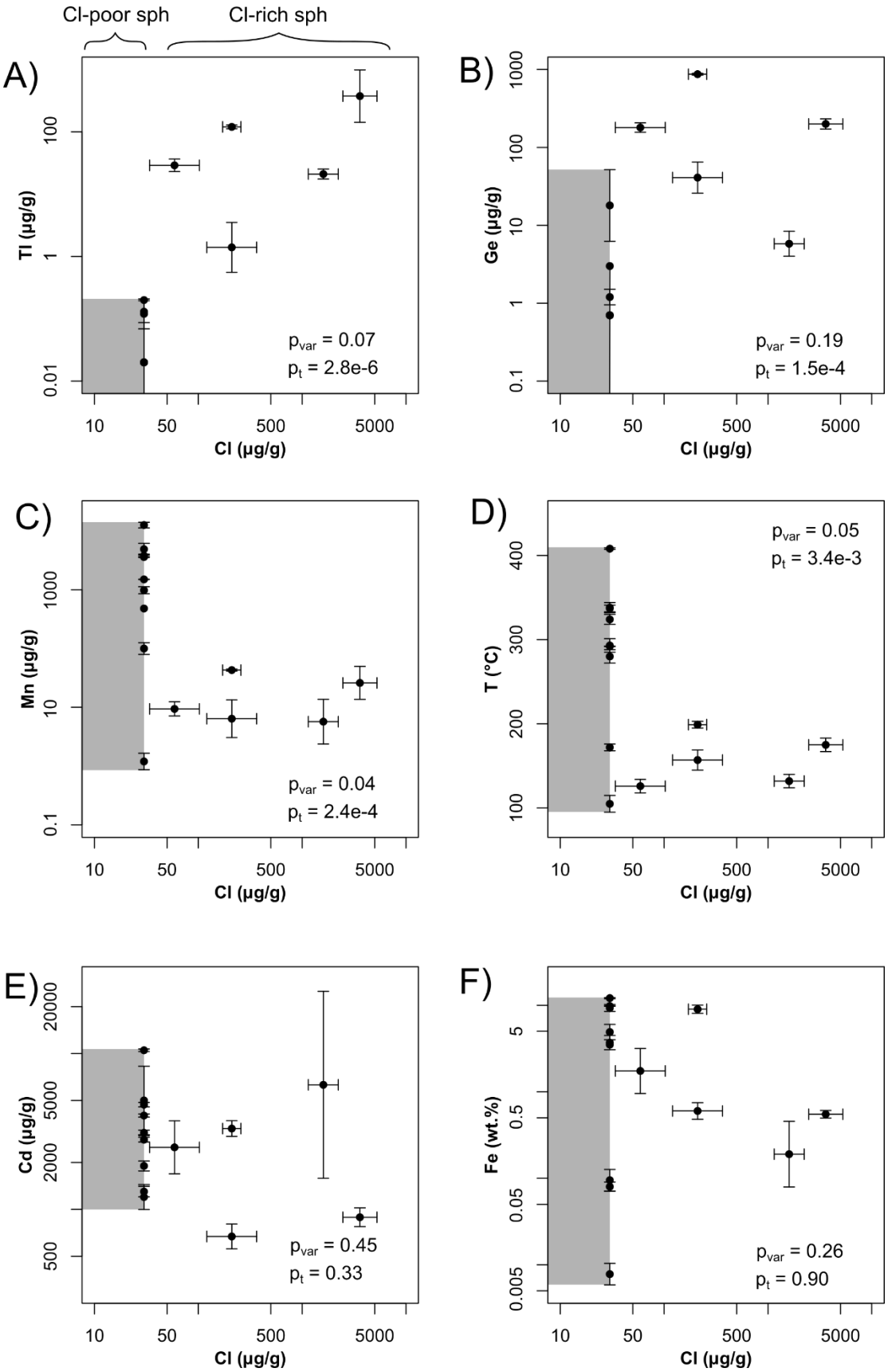

Fig. DR3: Cross-sample trends in trace-element concentrations as a function of Cl content: A) Tl, B) Ge, C) Mn, D) GGIMFis temperature, E) Cd, F) Fe. Individual points show geometric means with 95% confidence intervals. Fe, Cd and Cl concentrations were determined by EPMA measurements, while Tl, Ge and Mn are from LA-ICP-MS measurements. The two p-values are defined as follows: p_{var} corresponds to the p-value for the equal-variance test, p_t to the p-value for the student's t-test. For those cases in which $p_{var} > 0.05$, we assumed equal variance of the two populations for the t-test.

303

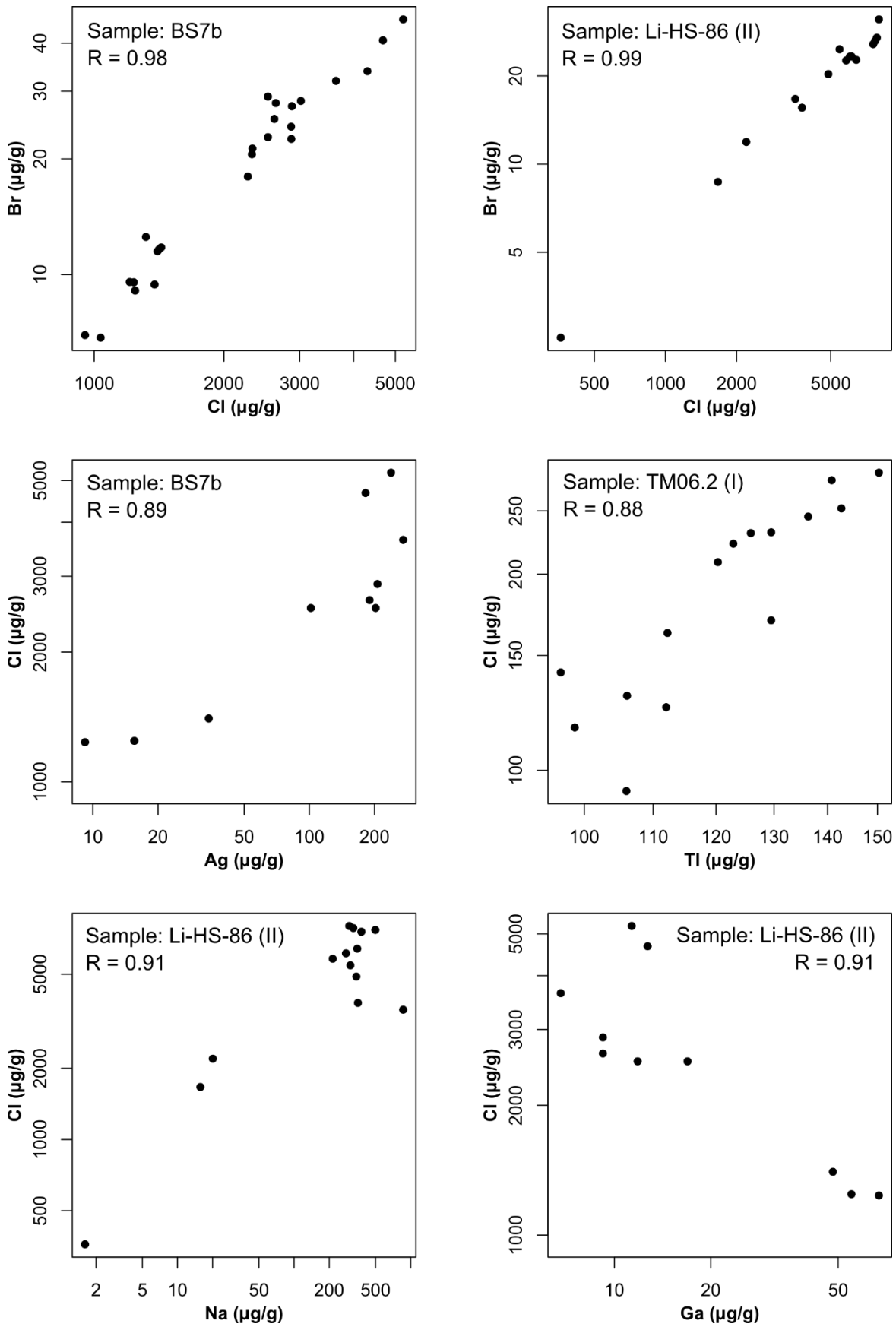

304

305 **Fig. DR4:** Scatter plots for different trace element-chlorine pairs from Table DR9.

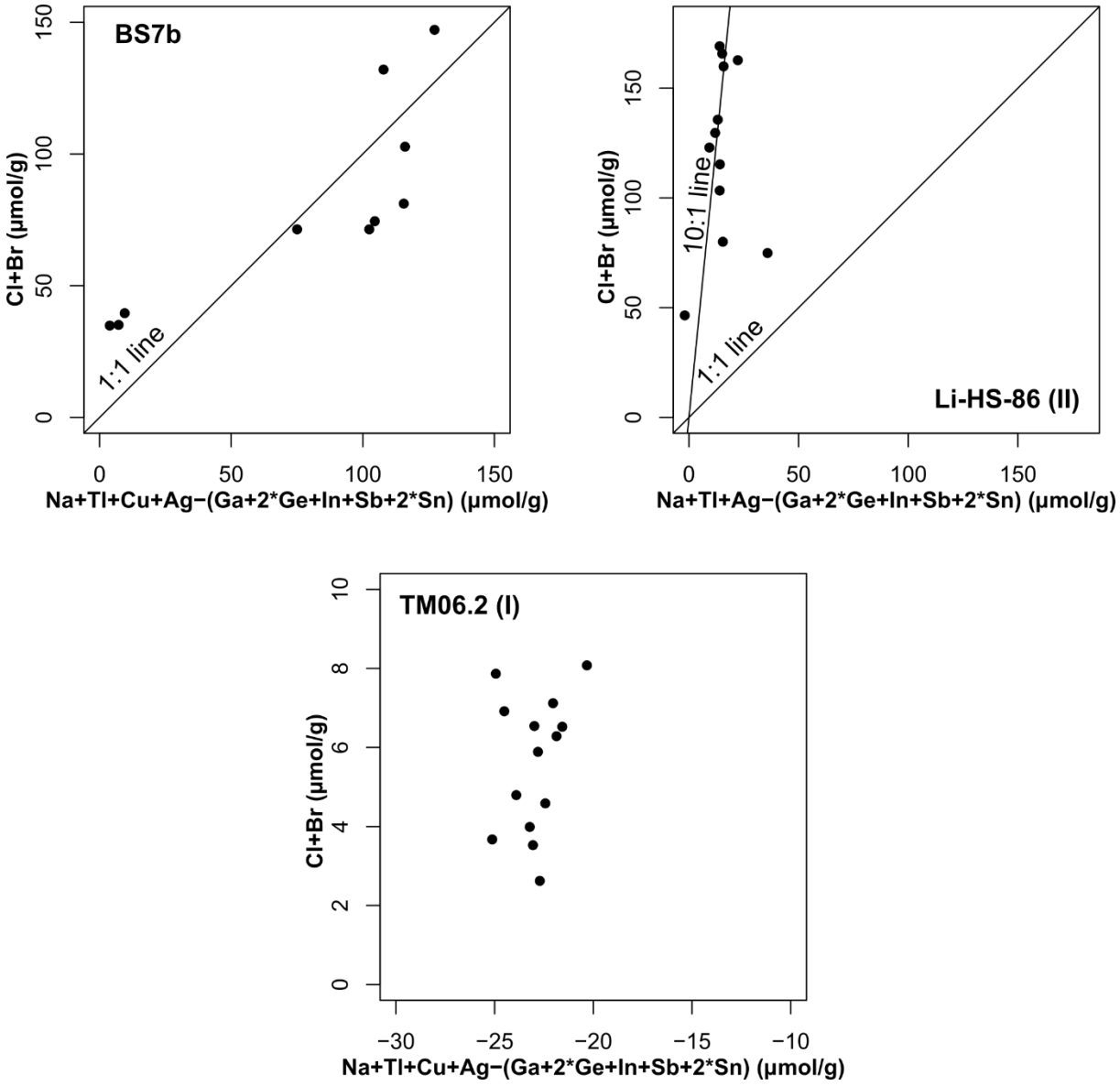

306

307 **Fig. DR5:** Scatter plots of Cl content against charge balance of cations for sphalerite analyses on Cl-rich samples. Charge
308 balances are calculated as the sum of cations probably present as univalent species (Na, Tl, Cu, Ag), minus the sum of cations
309 probably present as either trivalent or tetravalent species (Ga, Ge, In, Sb, Sn) (cf. Belissont et al., 2014). In sphalerite
310 Li-HS-86 (II), Cu concentration was not considered, since the Cu is probably present in inclusions, not the lattice (cf. Fig. DR8
311 and section DR2.6 below). Cl concentrations in Li-HS-86 (II) were also corrected for the proportion likely hosted in Cu-Pb-Cl
312 inclusions (see below).

313

314

315 **2.4 EPMA maps**

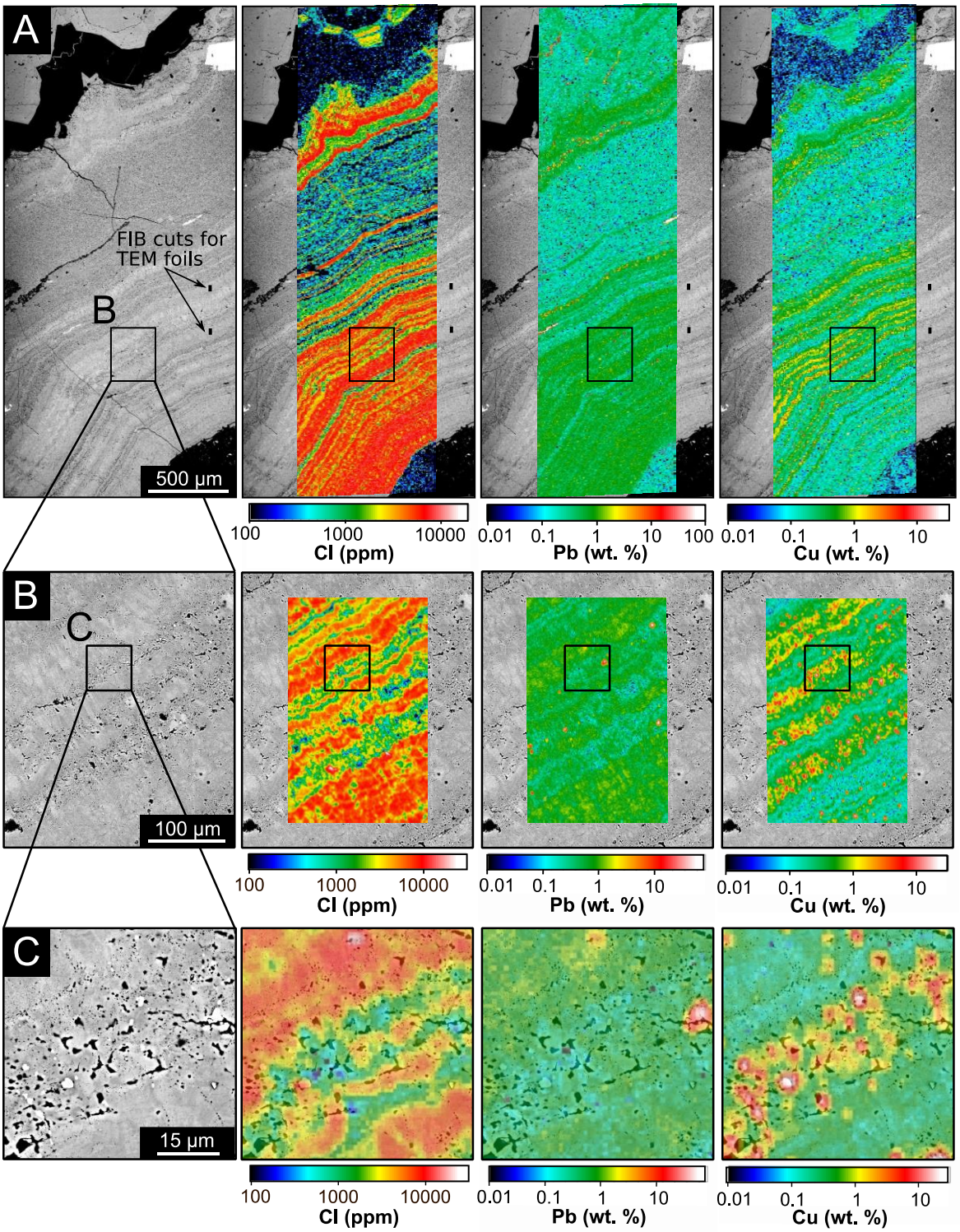

316

317 **Fig. DR6:** EPMA maps at different scales for sample Li-HS-86 (sph II) showing Cl, Pb, and Cu distribution, superimposed on
318 high-contrast BSE images of the polished sample surface: A) mm-scale distribution, B) intermediate scale, C) micron-scale.

319

320

321

2.5. STEM-EDX examination of samples

Micrographs and EDX maps of a selected area on sample BS7b are shown in Fig. 2 in the main text. For the corresponding material for sample Li-HS-86 see Fig. DR7. Tables DR10 and DR11 summarize the compositions of different mapped areas on both samples, based on the summed EDX spectra. Note that this EDX data is only semi-quantitative. High background Cu concentrations are due to secondary fluorescence radiation excited on the Cu-grids used to mount the samples. Sulfur concentrations were systematically underestimated, while concentrations of other elements were in reasonable agreement with EPMA measurements. The approximate molar ratio of Cu:Pb:Cl in the Cl-rich inclusions in sample Li-HS-86 is 4:1:2 (corrected for spurious Cu-concentrations). This is not compatible with any known mineral species. Unfortunately, the small size of the inclusions did not permit further investigation.

Table DR10 – Compositions of different map areas in Fig. DR7 from STEM-EDX

	Zn (wt. %)	S (wt. %)	Fe (wt.%)	Cu (wt.%)	Pb (wt.%)	Cl (wt. %)	Sum (wt.%)
Whole map	69 ± 11	15 ± 3	0.8 ± 0.1	14 ± 2	0.37 ± 0.05	0.20 ± 0.04	99
Area 1	69 ± 11	15 ± 3	0.8 ± 0.1	13 ± 2	0.41 ± 0.06	0.10 ± 0.02	99
Area 2	57 ± 9	13 ± 3	0.8 ± 0.1	20 ± 3	5.2 ± 0.7	2.2 ± 0.4	99

Table DR11 – Composition of map area in Fig. 2 (main text) from STEM-EDX

	Zn (wt. %)	S (wt. %)	Fe (wt.%)	Cd (wt.%)	Cu (wt.%)	Pb (wt.%)	Cl (wt. %)	Sum (wt.%)
Whole map	60 ± 9	22 ± 2	0.2 ± 0.03	1.2 ± 0.2	15 ± 2	0.31 ± 0.04	0.27 ± 0.05	99

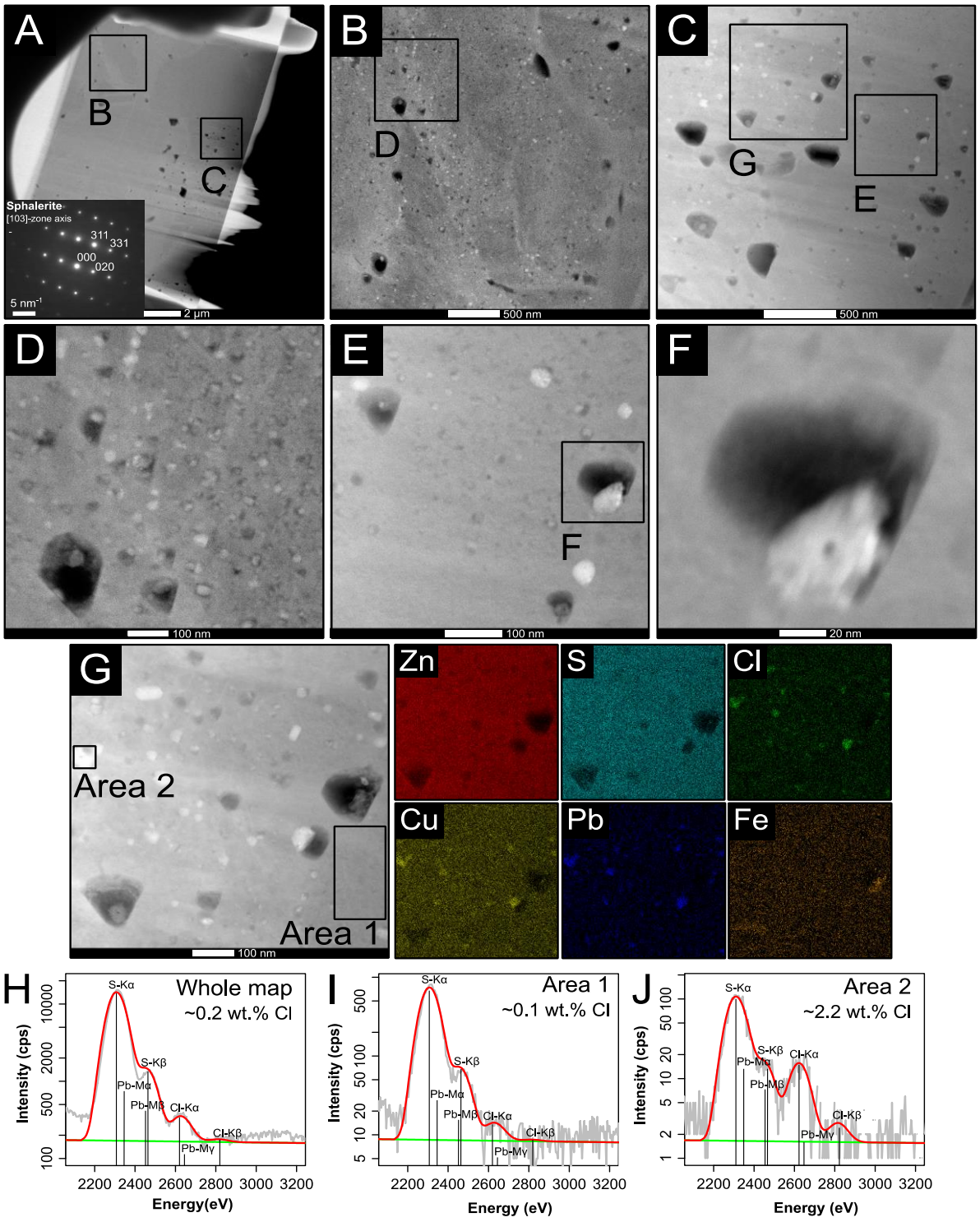

Fig. DR7: Summary of STEM and STEM-EDX imaging in sample Li-HS-86 (sph II): A) overview of sample foil with corresponding SAED pattern in lower left-hand corner; B) and C) detailed HAADF-STEM images of A) as indicated; D) detail of B) showing close-up of nano-porosity; E) detail of C) showing inclusions; F) detail of E) showing close-up of inclusion hosted in nano-pore; G) detail of C) and EDX maps of same area; H), I) and J) summed EDX spectrum for different parts of the map area shown in G) as indicated (grey line – data, red line – fitted spectrum, green line – fitted background). Note complex nanostructure of the material (different domains, pores, bright inclusions) and high Cl contents hosted in bright inclusions as well as sphalerite matrix.

2.6. Estimation of Cl hosted in Cu-Pb-Cl inclusions in Li-HS-86

An estimate of the maximum amount of Cl hosted within Cu-Pb-Cl inclusions in sample Li-HS-86 can be made using the results of LA-ICP-MS measurements, assuming that all of the Cu and Pb is hosted in Cl-rich inclusions as follows:

$$Cl_{incl} = (2 * Cu + 0.5 * Pb)/2$$

where concentrations are in µmol/g. The ratio in which Cu and Pb enter the equation is equal to that estimated from the Cl-rich inclusions via STEM-EDX studies (cf. Table DR10). Since the sphalerite also contains inclusions of tennantite and galena, this will tend to overestimate the amount of Cl in inclusions.

Nevertheless, Fig. DR8a shows that Cu and Pb are present in the sphalerite mostly in the same ratio as that observed for the inclusions. This indicates that the greater part of these two elements is present in the inclusions. Finally, Fig. DR8b is a plot of the estimated Cl concentrations hosted in inclusions versus total Cl concentration. This indicates that only about one quarter of the Cl is hosted in these inclusions.

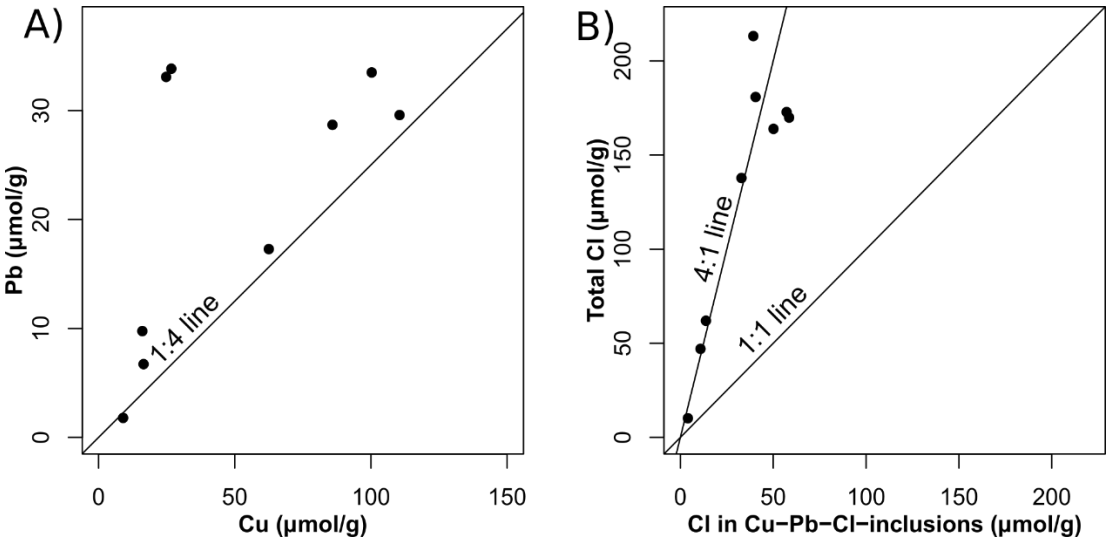

Fig. DR8: Estimation of proportion of Cl hosted in Cu-Pb-Cl inclusions in sample Li-HS-86: A) scatter plot of Pb vs. Cu concentrations, indicating that for most measurement points, the two elements are present in a 4:1 ratio, the same as in the Cu-Pb-Cl inclusions; B) scatter plot of total Cl vs. estimated Cl in Cu-Pb-Cl inclusions, indicating that only about 25% of total Cl is hosted in these inclusions.

3. Probable substitution mechanisms for lattice-hosted Cl and Br

The fact that substantial concentrations of Cl (and probably Br) are present as atomic-scale substitutions in sphalerite raises the question how substitution for S is accommodated. Since Cl^- and Br^- ions probably substitute for sulfide ions, their incorporation is expected to introduce a net positive charge on the sphalerite crystal lattice. Therefore, a compensation mechanism is required to maintain charge balance. There are two potential candidates for such a mechanism:

1) **Coupled substitution**, where the introduction of Cl^- (or Br^-) is accompanied by the exchange of Zn^{2+} for a monovalent cation A^+ (e.g. Cu^+, Ag^+, Tl^+), such that:

$$ZnS_{sph} + Cl^-_{aq} + A^+_{aq} \leftrightarrow ACl_{sph} + Zn^{2+}_{aq} + S^{2-}_{aq} \quad (1)$$

where the subscripts aq and sph denote the hydrothermal fluid and the sphalerite solid solution, respectively.

2) **Vacancy generation**, where a vacancy is created to compensate for two substituted Cl^- ions:

$$2\ ZnS_{sph} + 2\ Cl^-_{aq} \leftrightarrow 2\ ZnCl^+_{sph} + \square S^{2-}_{sph} + S^{2-}_{aq} \quad (2)$$

Here, $\square S^{2-}_{sph}$ denotes a Zn vacancy.

Several studies have shown that equivalent compensation mechanisms can explain the substitution of tri- and tetravalent cations for Zn^{2+}, which would otherwise also introduce a net positive lattice charge (e.g. Cook et al., 2012; Cook et al., 2015; Belissont et al., 2016).

To test which mechanism is most likely to be relevant in the investigated samples, we plotted the net negative charge introduced into the sphalerite by mono-, tri- and tetravalent cations against Cl + Br concentrations (Fig. DR5). This showed that approximate charge balance is only maintained in sample BS7b, indicating coupled substitution as the main incorporation mechanism. In samples Li-HS-86 and TM06.2 on the other hand, there are large imbalances between the net lattice charges introduced by substituting cations and anions, indicating incorporation of Cl^- and Br^- by Zn-vacancy generation. This would be consistent with available XANES data for Ge in TM06.2 (Cook et al., 2015).

While similar charge balance plots have been used in previous studies to check for coupled substitution (e.g. Johan, 1988; Belissont et al., 2014), we note that these studies generally omitted Cl and Br. Given the presence of high Cl concentrations in some sphalerites, the previous conclusions derived from such plots regarding the incorporation mechanisms of e.g. Ge into the sphalerite lattice may therefore be erroneous and require re-examination in light of our new results.

References

Armstrong, J.T., 1988, Quantitative analysis of silicate and oxide minerals: Comparison of Monte Carlo, ZAF, and ϕ(ρz) procedures *in* Newbury, D.E., ed., Microbeam Analysis, San Fransisco Press, p. 239-246.

Bauer, M., Burisch, M., Ostendorf, J., Krause, J., Frenzel, M., Seifert, T., and Gutzmer, J., 2019, Trace element geochemistry of sphalerite in contrasting hydrothermal fluid systems of the Freiberg district, Germany: insights from LA-ICP-MS analysis, near-infrared light microthermometry of sphalerite-hosted fluid inclusions, and sulfur isotope geochemistry: Mineralium Deposita, v. 54, p. 237-262.

Belissont, R., Boiron, M.-C., Luais, B., and Cathelineau, M., 2014, LA-ICP-MS analyses of minor and trace elements and bulk Ge isotopes in zoned Ge-rich sphalerites from the Noailhac – Saint-Salvy deposit (France): Insights into incorporation mechanisms and ore deposition processes: Geochimica et Cosmochimica Acta, v. 126, p. 518-540.

Ciobanu, C.L., Cook, N.J., Utsunomiya, S., Pring, A., and Green, L., 2011, Focussed ion beam-transmission electron microscopy applications in ore mineralogy: Bridging micro- and nanoscale observations: Ore Geology Reviews, v. 42, p. 6-31.

Cook, N.J., Ciobanu, C.L., Pring, A., Skinner, W., Shimizu, M., Danyushevsky, L., Saini-Eidukat, B., and Melcher, F., 2009, Trace and minor elements in sphalerite: A LA-ICP-MS study: Geochimica et Cosmochimica Acta, v. 73, p. 4761-4791.

Donovan, J.J., and Rowe, M., 2005, Techniques for Improving Quantitative Analysis of Mineral Glasses: Geochimica et Cosmochimica Acta, suppl. 69 (10), Goldschmidt abstracts.

Donovan, J.J., and Tingle, T.N., 1996, An Improved Mean Atomic Number Background Correction for Quantitative Microanalysis: Microscopy and Microanalysis, v. 1, p. 1-7.

Donovan, J.J., Singer, J.W., and Armstrong, J.T., 2016, A new EPMA method for fast trace element analysis in simple matrices: American Mineralogist, v. 101, p. 1839-1853.

Ehrig, K., McPhie, J., and Kamenetsky, V.S., 2012, Geology and mineralogical zonation of the Olympic Dam iron oxide Cu-U-Au-Ag deposit, South Australia: Society of Economic Geologists Special Publication, v. 16, p. 237-268.

Frenzel, M., Hirsch, T., and Gutzmer, J., 2016, Gallium, germanium, indium, and other minor and trace elements in sphalerite as a function of deposit type – A meta-analysis: Ore Geology Reviews, v. 76, p. 52-78.

Hammerli, J., Rusk, B., Spandler, C., Emsbo, P., and Oliver, N.H.S., 2013, In situ quantification of Br and Cl in minerals and fluid inclusions by LA-ICP-MS: A powerful tool to identify fluid sources: Chemical Geology, v. 337, p. 75-87.

Hitzman, M.W., Redmond, P.B., and Beaty, D.W., 2002, The carbonate-hosted Lisheen Zn-Pb-Ag deposit, County Tipperary, Ireland: Economic Geology,v. 97, p. 1627-1655.

Jansson, N.F., Zetterqvist, A., Allen, R.L., Billström, K., and Malmström, L., 2017, Genesis of the Zinkgruvan stratiform Zn-Pb-Ag deposit and associated dolomite-hosted Cu ore, Bergslagen, Sweden: Ore Geology Reviews, v. 82, p. 285-308.

Kalogeropoulos, S.I., Kilias, S.P., and Bitzios, D.C., 1989, Genesis of the Olympias carbonate-hosted Pb-Zn(Au,Ag) sulfide ore deposit, Eastern Chalkidiki Peninsula, Northern Greece: Economic Geology, v. 84, p. 1210-1234.

Lombaard, A.F., Günzel, A., Innes, J., and Krüger, T.L., 1986, The Tsumeb lead-zinc-copper-silver deposit, South West Africa / Namibia *in* Annhaeusser, C.R., and Maske, S., eds., Mineral Deposits of Southern Africa, Geological Society of South Africa, Johannesburg, p. 1761-1782.

Marks, M.A.W., Kendrick, M.A., Eby, G.N., Zack, T., and Wenzel, T., 2016, The F, Cl, Br and I contents of reference glasses BHVO-2G, BIR-1G, BCR-2G, GSD-1G, GSE-1G, NIST SRM 610 and NIST SRM 612: Geostandards and Geoanalytical Research, v. 41, p. 107-122.

NIST, 2012, Certificate of analysis – Standard Reference Material 610 – Trace elements in glass. National Institute of Standards & Technology, Gaithersburg, USA.

Ohta, E., 1991, Polymetallic mineralization at the Toyoha Mine, Hokkaido, Japan: Mining Geology, v. 41, p. 279-295.

Oyman, T., Minareci, F., and Piskin, Ö., 2003, Efemcukuru B-rich epithermal gold deposit (Izmir, Turkey): Ore Geology Reviews, v. 23, p. 35-53.

Paton, C., Hellstrom, J., Paul, B., Woodhead, J., and Hergt, J., 2011, Iolite: Freeware for the visualization and processing of mass spectrometric data: Journal of Analytical Atomic Spectrometry, v. 26, p. 2508-2518.

Saini-Eidukat, B., Melcher, F., and Lodziak, J., 2009, Zinc-germanium ores of the Tres Marias Mine, Chihuahua, Mexico: Mineralium Deposita, v. 44, p. 363-370.

Seo, J.H., Zajacz, Z. , 2016, Fractionation of Cl/Br during fluid phase separation in magmatic-hydrothermal fluids: Geochimica et Cosmochimica Acta, v. 183, p. 125-137.

Seo, J.H., Guillong, M., Aerts, M., Zajacz, Z., and Heinrich, C.A., 2011, Microanalysis of S, Cl, and Br in fluid inclusions by LA-ICP-MS: Chemical Geology, v. 284, p. 35-44.

461 Voudouris, P., Melfos, V., Spry, P.G., Bonsall, T., Tarkian, M., and Economou-Eliopoulos, M., 2008,
462 Mineralogical and fluid inclusion constraints on the evolution of the Plaka intrusion-related ore
463 system, Lavrion, Greece: Mineralogy and Petrology, v. 93, p. 79-110.

464 Wilson, S.A., Ridley, W.I., and Koenig, A.E., 2002, Development of sulfide calibration standards for the
465 laser ablation inductively-coupled plasma mass spectrometry technique: Journal of Analytical Atomic
466 Spectrometry, v. 17, p. 406-409.